PAPER

Check for updates

Energy-adaptive resistive switching with controllable thresholds in insulator–metal transition†

Tiantian Huang, [iD] ‡[ad] Rui Zhang,‡[ad] Lepeng Zhang,[c] Peiran Xu,[a] Yunkai Shao,[b] Wanli Yang,[a] Zhimin Chen, [iD] [c] Xin Chen*[abd] and Ning Dai [iD] [abd]

Resistive switching has provided a significant avenue for electronic neural networks and neuromorphic systems. Inspired by the active regulation of neurotransmitter secretion, realizing electronic elements with self-adaptive characteristics is vital for matching Joule heating or sophisticated thermal environments in energy-efficient integrated circuits. Here we present energy-adaptive resistive switching *via* a controllable insulator–metal transition. Memory-related switching is designed and implemented by manipulating conductance transitions in vanadium dioxide. The switching power decreases dynamically by about 58% during the heating process. Furthermore, the thresholds can be controlled by adjusting the insulator–metal transition processes in such nanowire-based resistive switching, and then preformed in a wide range of operating temperatures. We believe that such power-adaptive switching is of benefit for intelligent memory devices and neuromorphic electronics with low energy consumption.

Introduction

Advanced information devices are fundamental and required in intensive information data and modern electronic applications.[1–5] Resistive switching (RS) has exhibited excellent prospects in low operation power and flexible architecture towards neuromorphic techniques and artificial intelligence.[6–12] These neuromorphic RS have shown promise in deep learning,[13,14] autopilot systems,[15,16] and man–machine interaction systems.[17,18] Notably, the approximately 14 billion neurons in the human brain only have a power consumption of ~15 W.[19,20] It is still critical for realizing low energy consumption, high computing ability and ultrahigh storage density in such advanced bionic electronic devices. However, Joule heating is unavoidable and may result in redundant energy consumption.[21,22] In contrast to the low potential changes of sodium and potassium ions in nerve conduction,[23,24] the thermal effect induced by electronic transport may unquestionably alter switching behaviors in RS units. Recently, energy-adaptive devices have received huge attention and sparked

intense interest in advanced RS and energy-efficient components.[25–29] Active response and self-regulation will contribute to the realization of feedback, monitoring and passive control networks in natural neurons.[30–32]

Significantly, emergence of energy-adaptive is precisely to meet the requirements of complex environments, which highly require dynamic and controllable features. Unique insulator–metal transitions (IMT) has emerged in Mott insulators (*e.g.* VO_2, NbO_2),[33–36] and been recently adopted in the constructions of advanced RS devices. The IMT-based RS differs from those originated from redox in oxides or conductive filaments.[37,38] Extra fields (*e.g.* electric and thermal)[39–42] can induce an ultrafast resistance changing with multiple orders of magnitude.[43]

Here, we propose a switching power-adaptive RS with controllable thresholds towards intelligent memories. Diverse conductivity states get regulated though the electro-excited IMT process in VO_2 nanowires (VO_2-NWs). Variable thresholds show adaptability to the fluctuating thermal field, and correspondingly decreased switching power may effectively depress energy consumption and Joule heating. Moreover, energy-adaptive can be manipulated at higher operating temperature by adjusting field-dependent IMT processes in VO_2-NWs. We believe that energy-adaptive switching will provide more opportunities for designing and implementing advanced in-memory and neuromorphic components with low power consumption.

Results and discussion

Fig. 1a and b illustrated the principles of operation of the power-adaptive RS. To match the varied temperature induced by

[a]State Key Laboratory of Infrared Physics, Shanghai Institute of Technical Physics, Chinese Academy of Sciences, Shanghai 200083, China. E-mail: xinchen@mail.sitp.ac.cn

[b]Hangzhou Institute for Advanced Study, University of Chinese Academy of Sciences, Hangzhou 310024, China

[c]College of Materials Science and Engineering, Zhengzhou University, Zhengzhou 450052, China

[d]University of Chinese Academy of Sciences, Beijing, 100049, China

‡ T. Huang and R. Zhang contributed equally to this work.

RSC Advances

Joule heating, the self-adjusting RS got introduced *via* IMT characteristic. Here we simulated the low and high Joule heating by adjusting the working temperature. In an adaptive process of power-scaling, the corresponding working power decreases from P_{T_1} to P_{T_2} when the working temperature related with Joule heating increases from T_1 to T_2.

Joule heating related temperature (T_{RS}) could be quantitatively determined and then generally analyzed by the heat equation:[44]

$$C\frac{dT_{RS}}{dt} = P + k(T_0 - T_{RS}) \qquad (1)$$

where C was the heat capacitance of the VO$_2$ nanowire, P was the working power of the RS, T_0 was assigned to the (measured)
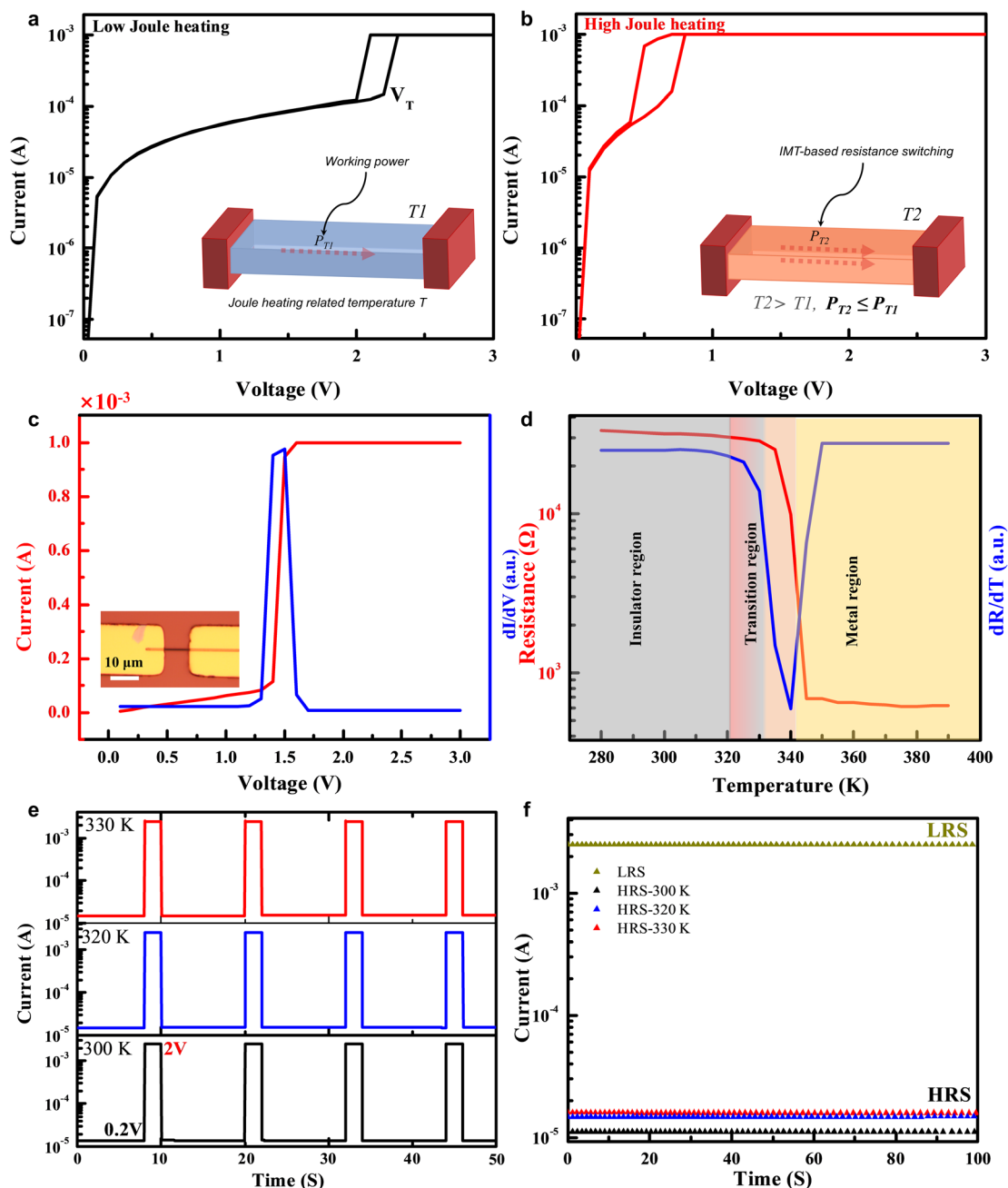

Fig. 1 IMT-based power-adaptive RS in (a) low and (b) high Joule heating environment simulated by low and high temperatures respectively. The insert schematic images represented the effect of Joule heating induced by working power on the temperature. (c) Electrically excited RS (red line) and the differential conductance dI/dV (blue line). The insert image represented the optical microscopy photograph of the two-terminal device based on VO$_2$-NW. (d) Thermal excited RS in VO$_2$-NW (red line) and related derivative of the resistance (blue line). (e) Cycles of RS under a pulsed voltage of 2 V with a period of 12 s at 300 K, 320 K and 330 K. (f) Retention property of HRS and LRS under different working temperatures.
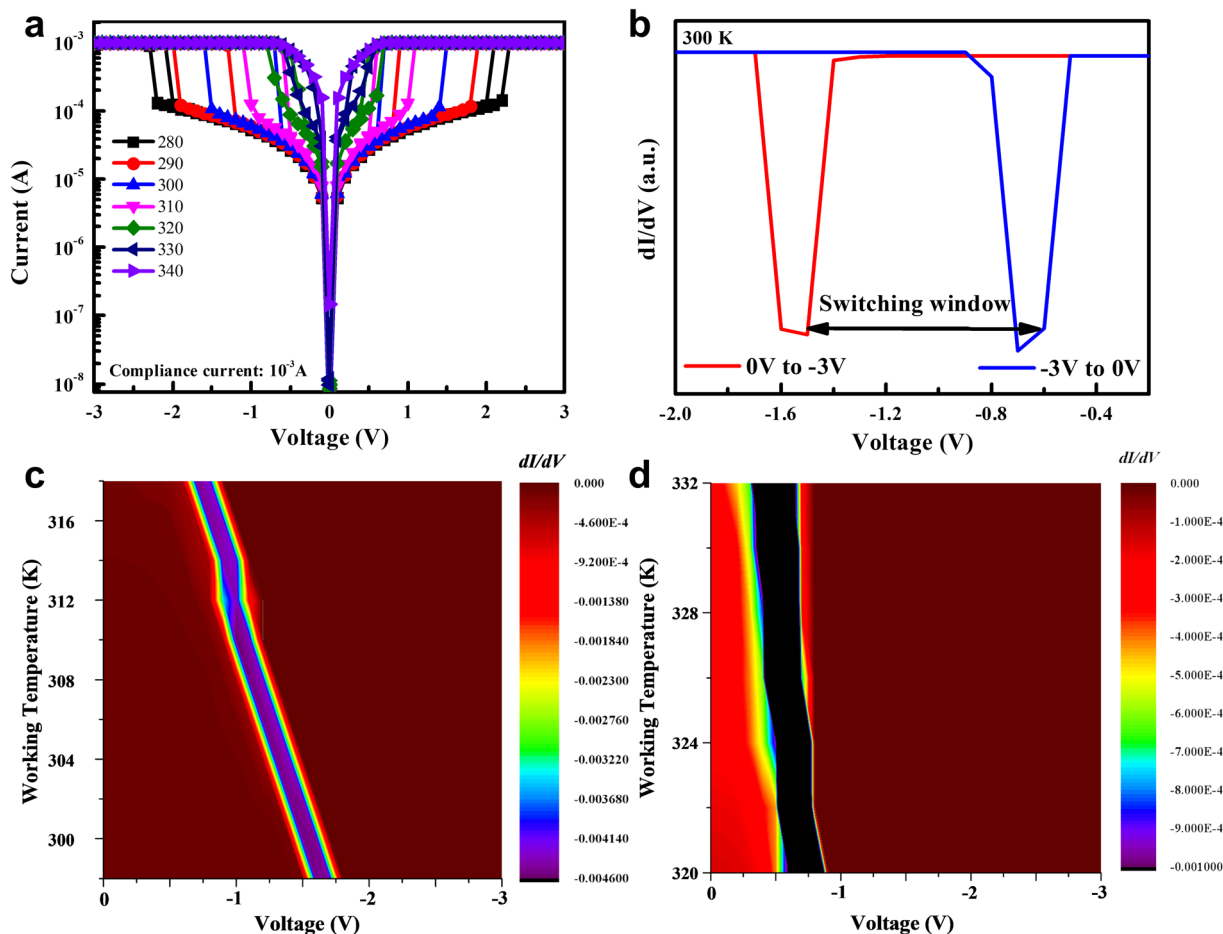
Fig. 2 (a) Current–voltage characteristics of the two-terminal device at different working temperatures with compliance current of 10^{-3} A. (b) The differential conductance dI/dV at 300 K. (c and d) Maps of differential conductance (dI/dV) as a function of the temperature and bias voltage. Boundary between bright and dark red region indicated critical point of the variable conductance. The sweeping voltage direction was from 0 V to −3 V (c) insulator region and (d) transition region under a compliance current of 10^{-3} A.

substrate temperature and κ was the thermal coupling constant between the substrate and the nanowire. In the equilibrium state $\left(\frac{\mathrm{d}T_{RS}}{\mathrm{d}t} = 0\right)$, the eqn (1) could be transformed into the following forms:

$$T_{RS} = \frac{P}{k} + T_0 \qquad (2)$$

From the eqn (2), the adaptive reduced switching power might produce a low T_{RS} through an effectively feedback regulation. And such negative feedback was benefit for reducing the energy dissipation.

The IMT-based RS behaviors got confirmed under both electric and thermal fields as shown in Fig. 1c and d. The insert image of Fig. 1c illustrated the two-terminal RS device constructed with VO$_2$-NW and gold electrodes. We also confirmed the fine lattice structure and components in VO$_2$-NW used for the construction of IMT-based RS by scanning electron microscope, Raman spectroscopy, X-ray diffraction spectroscopy and X-ray photoelectron spectroscopy. Here, the switching devices

were fabricated on the silica/silicon substrates in our cases. In a typical RS device, we used the crystalline nanowires with a length of about 50 μm and a width of around 200 nm (Fig. S1†). The monoclinic VO$_2$ is verified by Raman shifts at 195, 225 and 617 cm^{-1} (Fig. S2a†), and help for producing an obvious resistance changing.[45–47] In addition, a good crystallization and a preferred orientation of (011) plane were found in VO$_2$-NW (Fig. S2b and c†).[48–52] All these were helpful for the realization of a single-domain IMT process and the regulation of electron transport in the VO$_2$-NWs.[53] Fig. 1c and d illustrated that there were three different regions with changed conductance states, $i.e.$, insulator region, transition region and metal region in a typical IMT process. Symmetrical electrodes with chrome and gold were adopted to inhibit heating caused by undesired rectification effect, and then ohmic contact was confirmed by the current voltage curves in Fig. S3.† The electric-related behaviors of IMT-based RS were further observed in the insulator/transition regions (Fig. 1c). In these cases, a compliance current of 10^{-3} A was set to protect the device from breakdown under high potential. Moreover, the time-dependence of the fabricated RS was carried out under

a

Legend:
- Strong electronic correlation region
- Insulator region
- Linear Fit

$V_T = -6.75 + 0.02286T$
$V_T = -14.81 + 0.04446T$

Working Temperature (K) / **Threshold Voltage (V)**

b

$V_T = 1.40V$
$V_T = 0.60 V$

302 K
322 K

Voltage (V) / **Current (A)**

c

$T_0 = 298$ K
$T_0 = 332$ K

Power (W) / **Resistance (ohm)**

d

$\times 10^{-4}$

Switching Power of iusulator region
Switching Power of Strong electronic correlation region
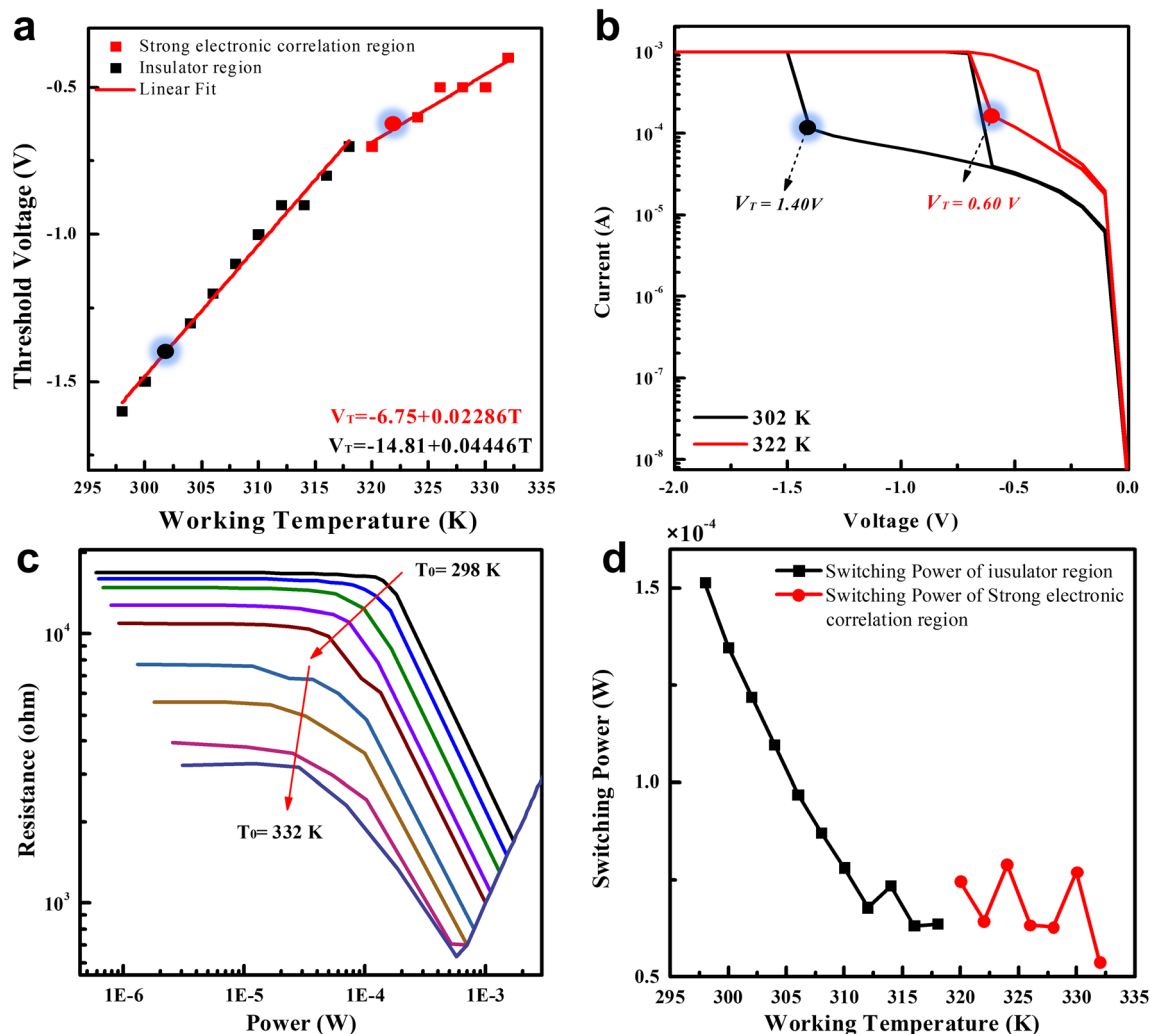
Working Temperature (K) / **Switching Power (W)**

Fig. 3 (a) The experimental (black discrete square) and the fitting curve (red solid lines) of threshold value as a function of the working temperature. (b) Sweeping current–voltage characteristics at 302 K and 322 K. (c) Resistance–power curves acquired at different working temperatures. (d) The functional relationship between working temperature and switching power.

voltage pulses with amplitude of 0.2 V and 2 V. In the wake of the increasing electric field strength, the high resistance state (HRS) abruptly switched to the low resistance state (LRS). As suggested in the inset in Fig. 1e, the electro-induced IMT-based RS was fast and repeatable when we simulated Joule heating and used a working temperature (300 K–330 K). The retention characteristics (Fig. 1f) of the resistance states were further investigated and verified at an operating temperature of 300 K, 320 K or 330 K. These three groups of temperatures were determined based on the insulation region and transition region as shown in Fig. 1d. Continuous stabilizations of the HRS and LRS kept a stable ON/OFF ratio about 10^3.

Subsequently, we further demonstrated the dynamic and thermal-adaptive thresholds of RS during IMT processes. Well-performed bidirectional resistive switching processes were illustrated in Fig. 2a. The sweeping voltage was from 0 V to −3 V, and then to 3 V, and finally to 0 V. From 280 K to 340 K, the threshold varied from 2.4 V to 0.3 V until the system completely turned into metallic state. Significantly, the IMT-based RS did

not require a forming process due to the carrier triggered Mott transition. The switching window about 1 V at 300 K was shown in Fig. 2b. And the enhanced electronic correlation in the transition region would make the switching window narrow. In order to understand such thermal-adaptive and controllable thresholds, we mapped the dynamic differential conductance as a function of the temperature and bias voltage. The slanted colored stripes indicated the minimum values of negative differential conductance, that was, the critical points of RS. The blue stripe represented the voltage range from the threshold to the corresponding voltage arriving at 10^{-3} A. The dI/dV maps with high contrast sharply displayed the linear trend of threshold value from 298 K to 318 K (Fig. 2c). A similar trend was also found in a transition region in a temperature range from 320 K to 332 K (Fig. 2d).

Critical threshold voltages were extracted for quantitative analysis about the thermal-adaptive thresholds. The voltage variations and a linear fitting were displayed in Fig. 3a when the operating temperature increased with a step of 2 K. For the
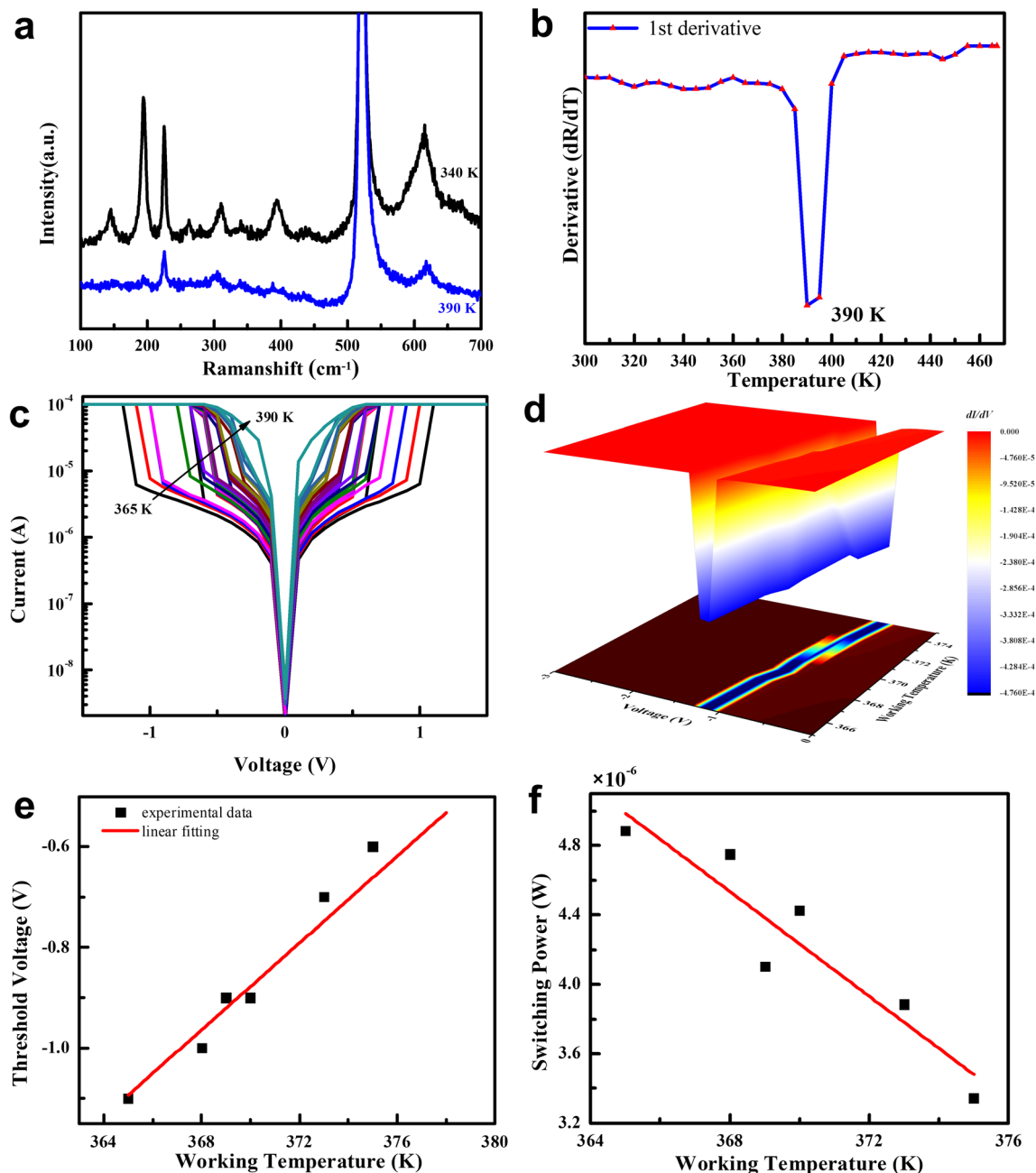
Fig. 4 (a) Raman spectra of the VO_2 nanowires deposited under different pressures. (b) Derivative resistance under variable temperatures of the two-terminal device based on VO_2 nanowires with a transition point of 390 K. (c) I–V curves of the two-terminal device based on VO_2 with a transition temperature of 390 K. (d) Map of differential conductance (dI/dV) as a function of the temperature and bias voltage. (e) Plots of threshold voltage and (f) switching power *versus* working temperature and the fitting curve (red solid lines).

insulator region from 298 K to 318 K, the varied thresholds matched an equation of $V_T = -14.81 + 0.04446T$. As a contrast, the equation of $V_T = -8.0 + 0.02286T$ was for the transition region from 320 K to 332 K. In insulator region, the small relative error R^2 of ~0.9877 revealed the high reliability and matching degree. Correlated thresholds varied from -1.7 V to -0.8 V. The step of 2 K corresponded to a threshold attenuation coefficient of about 0.090, while the related fitting threshold attenuation coefficient was about 0.089. As to the transition region, a R^2 of 0.8929 indicated a susceptible threshold in

strong electronic correlation region. Such difference was about 0.005 with a dynamic range of 0.3 V.

As to the cases at 302 K and 322 K, the measured thresholds were well agreement with the calculated one (Fig. 3b). The calculated $V_{T=302K}$ was -1.38 V while the measured is -1.40 V (the black dot in Fig. 3b). When the switching processes were performed in the transition region, the calculated $V_{T=322K}$ was -0.64 V while the measured with -0.60 V (the red dot in Fig. 3b). All these results indicated the universality of the fitting equations, and that the dynamic thresholds were thermal-

adaptive. Furthermore, the electrically induced IMT switching shown in Fig. 3c indicated trend of the varied power. From 1 μW to 10 μW, the stable resistance at different working temperatures revealed that stable thermal performance of the IMT-based switching. As shown by the red arrow, high operating temperature brought a skewed to the left of the resistance–power curves, that was, Joule heating for motivating switching got reduced. Corresponding to the enhancive Joule heating, increasing working temperature effectively reduced the switching power from 151.3 μW to 63.6 μW around 58.0% shown in Fig. 3d.

In the real and practical computing processes, a larger working temperature range of the thermal-adaptive RS was important and required because a higher frequency operation might induce a higher Joule heating and higher thermal fluctuation. Therefore, we attempted to construct a stable IMT-based RS worked at a higher operating temperature up to 390 K. As shown in Raman spectra in Fig. 4a, the weakening and blue shifts around 612 cm^{-1} indicated the increase of defects when we adjusted the defects in VO_2 nanowires by altering oxygen partial pressure. Such defects might lead to a higher transition temperature as displayed in Fig. 4b. In the range from 365 K to 390 K, the bidirectional switching processes were confirmed (Fig. 4c). Thermal-adaptive threshold voltages varied from −1.1 V to 0.6 V and finally to −0.4 V.

In Fig. 4d, the Map of differential conductance also suggested a linear function between the working temperature and bias voltage, which were similar with these illustrated in Fig. 3. The similar trend of the varied threshold indicated a stable reproducibility of the adaptive threshold voltages. Further analysis about the threshold voltage and switching power were displayed in Fig. 4e and f. A depressed switching power was from 4.8 μW to 4.2 μW. All these suggested the adaptive voltage and power scaling RS could be flexibly controlled and even programmed when we exploited the IMT processes in a widening range of operating temperature.

Furthermore, we analyzed the mechanism behind IMT-based energy-adaptive RS in briefly. It had been confirmed that the competition between coulomb repulsion energy and kinetic energy of the carrier determined the IMT process in strongly correlated system.[54] When the magnitude of external perturbation and coulomb repulsion energy were basically consistent, the delocalized carrier corresponded to the high kinetic energy of the increased density of free electrons would turn the system to be metal state.[55] In our case, the density of free electrons was directly related to field assisted carrier injection or increased working temperature. As to insulator region, the initial insulation state got quickly restored when bias voltage was removed. In the equilibrium state, the decreased thresholds corresponded to a stable resistance value of the same magnitude, that was, the energy used to excite the IMT got reduced. But for the transition region, coexisting insulating state and metallic state[56] promoted the delocalization energy to the same order of magnitude with coulomb repulsion energy. Higher ground states of kinetic energy got maintained accompanied by nonlinear attenuated resistances. With the decreased bias voltages, switching power also shown a nonlinear trend, and the system recovered to the intermediate state faster with a shrink hysteresis window.

Conclusions

In summary, we have demonstrated energy-adaptive RS with adjustable thresholds by the IMT features in VO_2 nanowires. The switching thresholds are electric-related and thermal-dependent while the IMT-based RS can also adapt to different thermal environments or temperature variations. The self-adjusted switching powers demonstrate a well performed energy-adaptive resistive switching. Ongoing investigations are carrying out for in-depth manipulating and understanding in VO_2 based energy-efficient memory. We think that such thermal-adaptive switching helps reduce energy consumption, and shows promise in the construction of advanced Mott memory and correlated in-memory devices.

Experimental section

Device fabrication

VO_2 nanowires were deposited on silica/silicon substrates as we previously reported.[51] Briefly, V_2O_5 powers were placed in the center of the quartz boat, and the clean substrate was placed downstream. The growth temperature was set at 900 °C, whereas the deposited time was about 20 minutes. UV lithography was then exploited to fabricate the device based on VO_2 nanowires while the channel length was about 10 μm. Metal electrodes (Au/Cr, 100/20 nm) were deposited by the thermal evaporation.

Device characterization

The morphology and microstructure of the grown VO_2 nanowires were characterized by Optical microscope (Nikon Cis), scanning electron microscope (FEI Sirion200), Raman spectroscope (Nanofinder 30) (TII Tokyo Instruments, Inc.), X-ray diffraction (D/MAX2200), and X-ray photoelectron spectroscopy (Thermo ESCALAB 250Xi) were adopted for the measurements. Electrical behaviors were recorded on a cryogenic probe station (Lakeshore TTPX) with a semiconductor characterization system. Under DC condition, we swept the bias voltage with 0.1 V step based on Keithley 2636B and LabVIEW-based I–V test software and the starting voltage was 0 V.

Conflicts of interest

There are no conflicts to declare.

Acknowledgements

References

1 B. Zhu, H. Wang, Y. Liu, D. Qi, Z. Liu, J. Yu, M. Sherburne, Z. Wang and X. Chen, *Adv. Mater.*, 2016, **28**, 1559–1566.

2 S. Chen, Z. Lou, D. Chen and G. Shen, *Adv. Mater.*, 2018, **30**, 1705400.

3 Z. Wei, K. Homma, K. Katayama, K. Kawai, S. Fujii, Y. Naitoh, H. Shima, H. Akinaga, S. Ito and S. Yoneda, *IEEE Trans. Electron Devices*, 2018, **65**, 5189–5194.

4 C. Wu, T. W. Kim, J. H. Park, B. Koo, S. Sung, J. Shao, C. Zhang and Z. L. Wang, *ACS Nano*, 2020, **14**, 1390–1398.

5 N. Vasileiadis, V. Ntinas, G. C. Sirakoulis and P. Dimitrakis, *Materials*, 2021, **14**, 5223.

6 C.-H. Huang, H. Chang, T.-Y. Yang, Y.-C. Wang, Y.-L. Chueh and K. Nomura, *ACS Appl. Mater. Interfaces*, 2021, **13**, 52822–52832.

7 M. Mirigliano, D. Decastri, A. Pullia, D. Dellasega, A. Casu, A. Falqui and P. Milani, *Nanotechnology*, 2020, **31**, 234001.

8 Y. van De Burgt, A. Melianas, S. T. Keene, G. Malliaras and A. Salleo, *Nat. Electron.*, 2018, **1**, 386–397.

9 Z. Wang, W. Zhao, W. Kang, Y. Zhang, J.-O. Klein, D. Ravelosona and C. Chappert, *Appl. Phys. Lett.*, 2014, **104**, 104.

10 S. Yu, B. Gao, Z. Fang, H. Yu, J. Kang and H. S. P. Wong, *Adv. Mater.*, 2013, **25**, 1774–1779.

11 L. Tong, Z. Peng, R. Lin, Z. Li, Y. Wang, X. Huang, K.-H. Xue, H. Xu, F. Liu, H. Xia, P. Wang, M. Xu, W. Xiong, W. Hu, J. Xu, X. Zhang, L. Ye and X. Miao, *Science*, 2021, **373**, 1353–1358.

12 M. D. Pickett, G. Medeiros-Ribeiro and R. S. Williams, *Nat. Mater.*, 2013, **12**, 114–117.

13 E. O. Neftci, *Iscience*, 2018, **5**, 52–68.

14 A. Sebastian, M. Le Gallo, R. Khaddam-Aljameh and E. Eleftheriou, *Nat. Nanotechnol.*, 2020, **15**, 529–544.

15 I. Astrov, S. Tatarly and S. Tatarly, *Adv. Electr. Comput. Eng.*, 2007, **7**, 18–22.

16 M. Aqib, R. Mehmood, A. Alzahrani, I. Katib, A. Albeshri and S. M. Altowaijri, *Sensors*, 2019, **19**, 2206.

17 K. S. Hale and K. M. Stanney, *IEEE Comput. Graph.*, 2004, **24**, 33–39.

18 J. Pei, L. Deng, S. Song, M. Zhao, Y. Zhang, S. Wu, G. Wang, Z. Zou, Z. Wu, W. He, F. Chen, N. Deng, S. Wu, Y. Wang, Y. Wu, Z. Yang, C. Ma, G. Li, W. Han, H. Li, H. Wu, R. Zhao, Y. Xie and L. Shi, *Nature*, 2019, **572**, 106–+.

19 C. Howarth, P. Gleeson and D. Attwell, *J. Cereb. Blood Flow Metab.*, 2012, **32**, 1222–1232.

20 C. Howarth, C. M. Peppiatt-Wildman and D. Attwell, *J. Cereb. Blood Flow Metab.*, 2010, **30**, 403–414.

21 J. J. Yang, F. Miao, M. D. Pickett, D. A. A. Ohlberg, D. R. Stewart, C. N. Lau and R. S. Williams, *Nanotechnology*, 2009, **20**, 215201.

22 H. Fangohr, D. S. Chernyshenko, M. Franchin, T. Fischbacher and G. Meier, *Phys. Rev. B: Condens. Matter Mater. Phys.*, 2011, **84**, 054437.

23 M. A. Leeves and F. McDonald, *Am. J. Orthod.*, 1995, **107**, 625–632.

24 N. Xu, *J. Membr. Biol.*, 2013, **246**, 75–90.

25 Y. Zhang, M. Khayatzadeh, K. Yang, M. Saligane, N. Pinckney, M. Alioto, D. Blaauw and D. Sylvester, *IEEE J. Solid-State Circuits*, 2018, **53**, 619–631.

26 H. Fuketa, M. Hashimoto, Y. Mitsuyama and T. Onoye, *IEEE T. VLSI Syst.*, 2012, **20**, 333–343.

27 H. Reyserhove and W. Dehaene, *IEEE J. Solid-State Circuits*, 2018, **53**, 2101–2113.

28 X. Hou, C. Liu, Y. Ding, L. Liu, S. Wang and P. Zhou, *Adv. Sci.*, 2020, **7**, 2002072.

29 A. Mraz, R. Venturini, D. Svetin, V. Sever, I. A. Mihailovic, I. Vaskivskyi, B. Ambrozic, G. Drazic, M. D'Antuono, D. Stornaiuolo, F. Tafuri, D. Kazazis, J. Ravnik, Y. Ekinci and D. Mihailovic, *Nano Lett.*, 2022, **22**, 4814–4821.

30 D. M. Blitz, *J. Neurophysiol.*, 2017, **118**, 949–963.

31 D. M. Blitz and M. P. Nusbaum, *J. Neurophysiol.*, 2012, **32**, 9182–9193.

32 C. Y. L. Huh, J. P. Peach, C. Bennett, R. M. Vega and S. Hestrin, *Curr. Biol.*, 2018, **28**, 114–120.

33 F. J. Morin, *Phys. Rev. Lett.*, 1959, **3**, 34–36.

34 S. H. Chang, S. B. Lee, D. Y. Jeon, S. J. Park, G. T. Kim, S. M. Yang, S. C. Chae, H. K. Yoo, B. S. Kang, M. J. Lee and T. W. Noh, *Adv. Mater.*, 2011, **23**, 4063–4067.

35 R. F. Janninck and D. H. Whitmore, *J. Phys. Chem. Solids*, 1966, **27**, 1183–1187.

36 S. Kim, J. Park, J. Woo, C. Cho, W. Lee, J. Shin, G. Choi, S. Park, D. Lee, B. H. Lee and H. Hwang, *Microelectron. Eng.*, 2013, **107**, 33–36.

37 J.-Y. Lee, Y.-J. Baek, Q. Hu, Y. J. Choi, C. J. Kang, H. H. Lee, H.-M. Kim, K.-B. Kim and T.-S. Yoon, *Appl. Phys. Lett.*, 2013, **102**, 122111.

38 X. Cao, Y. Han, J. Zhou, W. Zuo, X. Gao, L. Han, X. Pang, L. Zhang, Y. Liu and S. Cao, *ACS Appl. Mater. Interfaces*, 2019, **11**, 35914–35923.

39 Z. Li, Y. Guo, Z. Hu, J. Su, J. Zhao, J. Wu, J. Wu, Y. Zhao, C. Wu and Y. Xie, *Angew. Chem., Int. Ed.*, 2016, **55**, 8018–8022.

40 M. Nakano, K. Shibuya, D. Okuyama, T. Hatano, S. Ono, M. Kawasaki, Y. Iwasa and Y. Tokura, *Nature*, 2012, **487**, 459–462.

41 M. Liu, H. Y. Hwang, H. Tao, A. C. Strikwerda, K. Fan, G. R. Keiser, A. J. Sternbach, K. G. West, S. Kittiwatanakul, J. Lu, S. A. Wolf, F. G. Omenetto, X. Zhang, K. A. Nelson and R. D. Averitt, *Nature*, 2012, **487**, 345–348.

42 J. Cao, E. Ertekin, V. Srinivasan, W. Fan, S. Huang, H. Zheng, J. W. L. Yim, D. R. Khanal, D. F. Ogletree, J. C. Grossmanan and J. Wu, *Nat. Nanotechnol.*, 2009, **4**, 732–737.

43 J. Jian, X. Wang, L. Li, M. Fan, W. Zhang, J. Huang, Z. Qi and H. Wang, *ACS Appl. Mater. Interfaces*, 2017, **9**, 5319–5327.

44 S. Wang, W. Wei, T. Huang, T. Zhang, Z. Chen, L. Sun, H. Xia, T. Li, X. Chen, X. Chen, W. Lu and N. Dai, *Adv. Mater. Interfaces*, 2018, **5**, 1800374.

45 J. H. Parker, D. W. Feldman and M. Ashkin, *Phys. Rev.*, 1967, **155**, 712–714.

46 Y. Kalcheim, A. Camjayi, J. Del Valle, P. Salev, M. Rozenberg and I. K. Schuller, *Nat. Commun.*, 2020, **11**, 2985.

47 D. Bersani, P. P. Lottici and A. Montenero, *J. Raman Spectrosc.*, 1999, **30**, 355–360.

48 T. Huang, S. Wang, W. Wei, Y. Yang, W. Yang, M. Yuan, R. Zhang, T. Zhang, X. Chen, Y. Sun, X. Zhou, J. Shao, X. Chen and N. Dai, *Phys. Status Solidi B*, 2020, **257**, 1900785.

49 J. Mendialdua, R. Casanova and Y. Barbaux, *J. Electron Spectrosc. Relat. Phenom.*, 1995, **71**, 249–261.

50 G. Silversmit, D. Depla, H. Poelman, G. B. Marin and R. De Gryse, *J. Electron Spectrosc. Relat. Phenom.*, 2004, **135**, 167–175.

51 W. Wei, T. Huang, S. Wang, W. Luo, T. Zhang, W. Hu, X. Chen and N. Dai, *Phys. Status Solidi RRL*, 2019, **13**, 1900383.

52 S. Wang, W. Wei, T. Huang, T. Zhang, Z. Chen, X. Chen and N. Dai, *Adv. Eng. Mater.*, 2019, **21**, 1900947.

53 J. Wei, Z. Wang, W. Chen and D. H. Cobden, *Nat. Nanotechnol.*, 2009, **4**, 420–424.

54 N. F. Mott, *Phys. Soc. A*, 1949, **62**, 416–422.

55 Y. Zhou and S. Ramanathan, *Proc. IEEE*, 2015, **103**, 1289–1310.

56 M. M. Qazilbash, M. Brehm, B.-G. Chae, P. C. Ho, G. O. Andreev, B.-J. Kim, S. J. Yun, A. V. Balatsky, M. B. Maple, F. Keilmann, H.-T. Kim and D. N. Basov, *Science*, 2007, **318**, 1750–1753.

© 2022 The Author(s). Published by the Royal Society of Chemistry